PAPER

Check for updates

A simple and robust method to quantify exciton dissociation efficiency with high precision in non-fullerene organic solar cells

Jared Faisst, [ID] *[abc] Mathias List, [ID] [ac] Leonie Pap, [ID] [ac] Reid Patterson, [ID] [ac] Uli Würfel [ID] [ac] and Andreas W. Bett [ID] *[ab]

Exciton dissociation at donor–acceptor interfaces remains a critical bottleneck for charge generation in non-fullerene acceptor based organic solar cells (OSCs), yet its precise quantitative assessment is experimentally challenging. Here, we introduce a comparative framework that enables robust determination of the exciton dissociation efficiency η_{ED} by benchmarking a reference morphology against intentionally coarsened morphologies. The latter is achieved by increasing the acceptor content in the blend, thereby enlarging the acceptor domains. This leads to a rise in photoluminescence (non-dissociating fraction of excitons) and decrease in short-circuit current (dissociating fraction). By tracking the relative changes of both these fractions with respect to the photogeneration of excitons, constant prefactors cancel out, eliminating the need for absolute calibrations or numerical assumptions regarding charge-separation and charge-collection efficiencies. The method yields consistent exciton dissociation efficiencies of 96.2 ± 0.4% for D18:Y6 and 97.2 ± 0.6% for PM6:DTY6. A pragmatic fully experimental approach is also presented yielding lower bound estimates within 1% uncertainty. Comparison with conventional internal quantum efficiency analysis based on optical simulations confirms the physical validity of the framework while highlighting its markedly superior precision. The proposed methodology provides a broadly applicable tool for identifying dissociation-related losses in state-of-the-art OSCs and supports targeted morphology optimization for continued performance improvements.

Broader context

Organic photovoltaics (OPVs) are an emerging photovoltaic technology distinguished by their low material and energy demands, solution processability, and versatile application potential, including flexible and semi-transparent devices. The photoactive layer in OPVs consists of a blend of donor and acceptor materials (polymers and small molecules) that form an interpenetrating network. This architecture is required because light absorption initially generates tightly bound excitons, which must dissociate at donor–acceptor interfaces to produce free charge carriers and contribute to the photocurrent. The efficiency of this exciton dissociation process depends on multiple factors, such as the coarseness of the blend morphology, the exciton diffusion length, and the energetic landscape at the interface. Reliable quantification of the exciton dissociation efficiency is therefore essential for gaining insight into device performance and guiding further optimization. In this work, we present a novel experimental approach that enables quantification of this efficiency with an uncertainty an order of magnitude lower than that of conventional internal quantum efficiency–based estimates.

1. Introduction

Organic photovoltaics (OPVs) are a promising low-cost and low-energy-demanding solar technology.[1] Beyond recently surpassing the 20% power-conversion-efficiency threshold for opaque devices[2,3] and also reporting increased stability,[4] one of their most compelling advantages lies in their application versatility. Thanks to their tunable optoelectronic properties and strong absorption, OPVs are particularly attractive for lightweight, flexible, and semitransparent photovoltaic applications.[5–10]

A fundamental limitation of OPVs arises from the rather low relative permittivity of organic semiconductors ($\varepsilon_r \approx 3$–5),[11] in contrast to inorganic photovoltaic materials such as perovskites (≈ 18),[12] silicon (≈ 12),[13] and gallium arsenide (≈ 13).[14] As a consequence, excitons generated in the organic absorber materials experience a rather large Coulombic binding energy and do not dissociate effectively at room temperature. Efficient current generation in high-performance OPVs is therefore achieved by blending a donor polymer with a non-fullerene acceptor (NFA) to form a bulk heterojunction, with both

aFraunhofer Institute for Solar Energy Systems ISE, Heidenhofstr. 2, 79110 Freiburg, Germany. E-mail: jared.faisst@ise.fraunhofer.de

bInstitute of Physics, University of Freiburg, Hermann-Herder-Str. 3, 79104 Freiburg, Germany. E-mail: andreas.bett@ise.fraunhofer.de

cFreiburg Materials Research Center FMF University of Freiburg, Stefan-Meier-Str. 21, 79104 Freiburg, Germany

components absorbing complementary portions of the solar spectrum. The energetic offsets between donor and acceptor facilitate exciton dissociation: the deeper LUMO of the acceptor (higher electron affinity) promotes electron transfer of donor excitons, while the higher-lying HOMO of the donor (smaller ionization energy) facilitates hole transfer of acceptor excitons.[15,16]

The resulting exciton dissociation efficiency is strongly morphology-dependent. While larger domain sizes facilitate charge carrier transport, it can limit photogenerated excitons from reaching an interface leading to increased exciton recombination.[17] In modern NFA-based organic solar cells, donor excitons that do not reach an interface can still contribute to charge generation by transferring to the acceptor *via* Förster resonance energy transfer (FRET) and subsequently dissociating there.[18–22] This pathway is enabled by the spectral overlap between donor emission and acceptor absorption. Therefore, a higher emphasis is placed on the size of the acceptor domains which determine the effective exciton dissociation efficiency. The size of the domains can be controlled by chemically or thermally inducing aggregation behaviour of the planar structured NFA molecules.[23–32] Hence, a finely tuned and stable morphology is of high relevance in organic photovoltaic devices.[29,33]

Despite its importance as a metric for assessing bulk-heterojunction morphology, a precise experimental quantification of the exciton dissociation efficiency (η_{ED}) remains challenging and is typically only inferred indirectly from internal quantum efficiency measurements. In our previous work, we demonstrated that correlating changes in photocurrent and exciton photoluminescence enabled a quantitative determination of η_{ED} by comparing pristine devices with thermally coarsened morphologies.[34] This approach, however, relied on thermally inducible aggregation and is therefore not universally applicable.

In this work, we introduce a more general comparative methodology in which the exciton dissociation efficiency is extracted by systematically increasing the acceptor content to generate controlled variations in acceptor domain size. We demonstrate the approach on two state-of-the-art NFA systems with detailed error analysis and compare the obtained efficiencies to those derived from optical simulations, highlighting both the accuracy and practical advantages of the method.

2. Theoretical background

In organic solar cells, current generation proceeds through a sequence of steps. It begins with an incident photon flux, $\Phi_{ph}(\lambda)$, which is absorbed by the photoactive layer according to its spectral absorptance, $A_{PAL}(\lambda)$. The integrated product of $A_{PAL}(\lambda)$ and $\Phi_{ph}(\lambda)$ determines the total rate of exciton generation. The probability that these excitons reach a donor–acceptor interface and form a charge-transfer (CT) complex is given by the exciton dissociation efficiency, η_{ED}, while the probability that the CT complex subsequently dissociates into separated charge carriers (CS) is described by η_{CS}.[35] The resulting generated current density can therefore be expressed as:

$$J_{gen} = \eta_{ED}\eta_{CS}q\int_0^\infty A_{PAL}(\lambda)\Phi_{ph}(\lambda)\mathrm{d}\lambda \tag{1}$$

Excitons that are photogenerated outside their diffusion length L_D to a donor–acceptor interface recombine partially radiatively with an efficiency determined by the photoluminescence quantum yield (PLQY). Hence, the detected photoluminescence of excitons ($I_{lum,PE}$) is propotional to the fraction of non-dissociation ($\propto 1 - \eta_{ED}$) and can be described by

$$I_{lum,PE} = (1 - \eta_{ED})\frac{\Omega}{4\pi}\eta_{det}A_{det}\mathrm{PLQY}_{PE} \times \int_0^\infty A_{PAL}(\lambda)\Phi_{ph}(\lambda)\mathrm{d}\lambda \tag{2}$$

Here, Ω represents the solid angle of acceptance of the detector, η_{det} is the material and layer specific efficiency of detection that accounts for spectral sensitivity of the detector and the probability of emitted photons to leave the layer stack and A_{det} is the area observed by the detector. Calculating η_{ED} directly from either of the two equations poses the challenge of determining several experimental parameters that are often difficult to quantify reliably, such as the precise absorptance of the photoactive layer within the multilayer stack or the absolute emission and detection efficiencies required for photoluminescence analysis. To overcome this limitation, we propose an alternative approach that focuses on comparing devices with different morphologies, as introduced in our previous work.[34] This comparative method eliminates constant prefactors that affect both systems equally.

The central idea is sketched in Fig. 1. A reference morphology with an optimum donor:acceptor ratio is depicted, characterized by minimal 'dead volumes', *i.e.*, regions where excitons (on the non-fullerene acceptor) fail to reach a donor–acceptor interface and thus do not dissociate (detailed discussion including excitons on the donor phase will follow in section 3.2). Hence, the share of non-dissociation that is proportional to the PL (blue) is small compared to dissociation proportional to the generated current (yellow). For direct comparison, a coarsened morphology with larger domains is considered, which exhibits a reduced exciton dissociation efficiency η'_{ED}, and therefore a higher proportion of non-dissociating excitons. This leads to stronger PL emission and a correspondingly lower generated current density.

By postulating eqn (1) and (2) for (i) the reference morphology and (ii) the comparative morphology (denoted by a prime, ′) and dividing them, we obtain the normalized relationships:

$$j_{gen} = \frac{\eta'_{ED}}{\eta_{ED}}g_{PE} \tag{3}$$

$$i_{lum,PE} = \frac{1 - \eta'_{ED}}{1 - \eta_{ED}}g_{PE} \tag{4}$$

Here, the lowercase variables denote the relative change of the quantity in the comparative morphology relative to the value
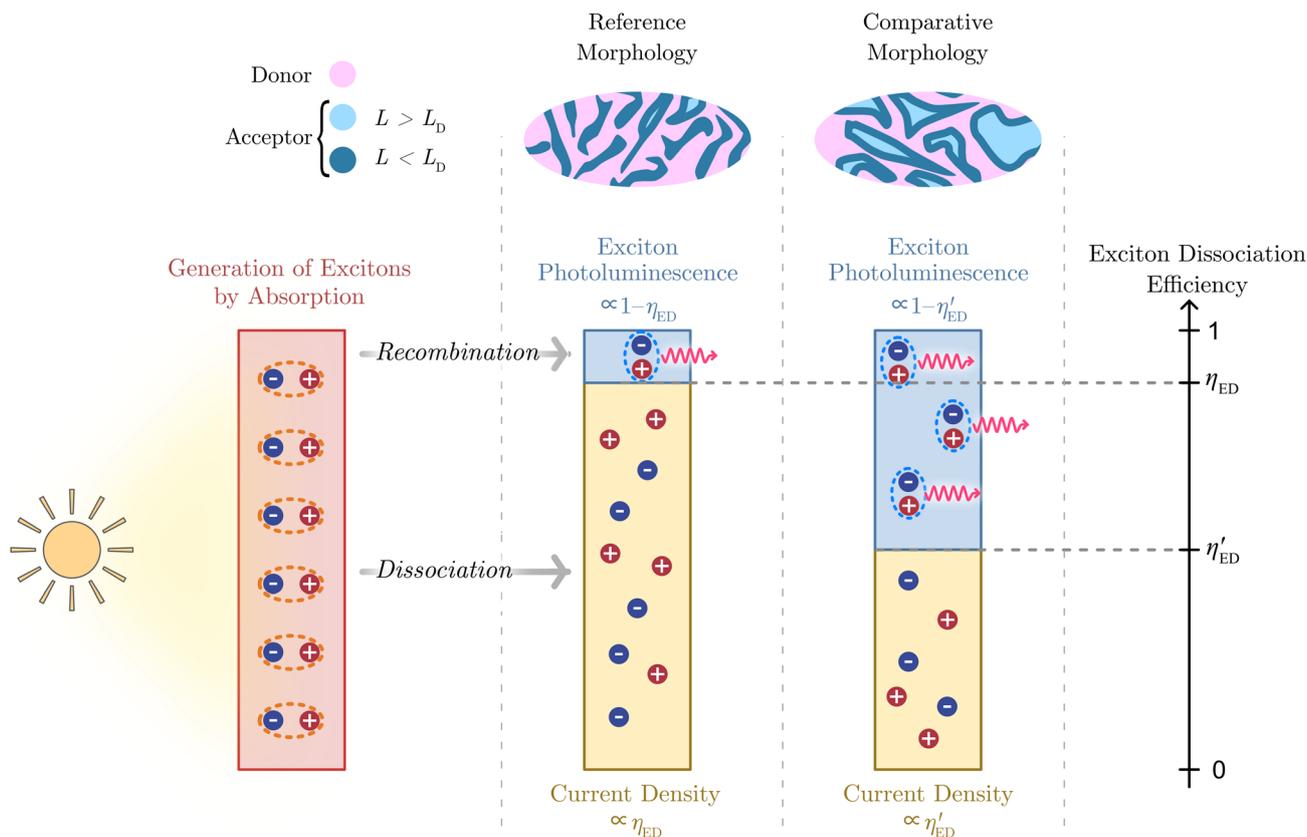
Fig. 1 Schematic illustration of the methodology used to estimate the exciton dissociation efficiency. Excitons are generated according to the optical absorption of the photoactive layer (red box) and can either recombine (partially radiatively), leading to photoluminescence (blue box), or dissociate into separated charge carriers that contribute to the photocurrent (yellow box). By comparing the photoluminescence and current density (both normalized to the exciton generation rate) for two distinct morphologies, the exciton dissociation efficiency can be directly determined for the reference morphology (η_{ED}) and for the comparative morphology (η'_{ED}).

obtained for the reference value. Specifically, $j_{gen} = J'_{gen}/J_{gen}$ is the normalized generated current density, $i_{lum,PE} = I'_{lum,PE}/I_{lum,PE}$ represents the normalized exciton photoluminescence, and

$$g_{PE} = \frac{\int_0^\infty A'_{PAL}(\lambda)\Phi_{ph}(\lambda)\mathrm{d}\lambda}{\int_0^\infty A_{PAL}(\lambda)\Phi_{ph}(\lambda)\mathrm{d}\lambda} \tag{5}$$

denotes the relative exciton generation rate. Importantly, all constant prefactors cancel in the normalization. This includes the $PLQY_{PE}$ given it can be described by a uniform value (detailed discussion provided in section 3.2) and η_{CS} as these quantities are independent of the morphology and depend instead on the intrinsic material properties and interfacial energetics, respectively. Solving both linearly independent equations for the two unknown exciton dissociation efficiencies, we obtain

$$\eta_{ED} = \frac{g_{PE} - i_{lum,PE}}{j_{gen} - i_{lum,PE}} \tag{6}$$

$$\eta'_{ED} = \frac{j_{gen}}{g_{PE}}\left(\frac{g_{PE} - i_{lum,PE}}{j_{gen} - i_{lum,PE}}\right) \tag{7}$$

3. Results and discussion

3.1. Reducing exciton dissociation by increasing acceptor concentration

To investigate the exciton dissociation efficiency of a bulk-heterojunction, the proposed methodology requires an additional device state with a coarsened morphology. In our previous work, such morphological alteration was induced by exposing the solar cells to accelerated thermal aging.[34] However, this approach is only of limited applicability, as it requires that phase separation can be induced by elevated temperature without compromising the chemical stability of the polymers and small molecules. In the present work, we present a more universally applicable approach for non-fullerene acceptor based organic solar cells, in which the morphological variation is achieved by altering the donor:acceptor ratio $r_{D:A}$, specifically, by increasing the acceptor content in the donor–acceptor blend. The effect of such compositional tuning is illustrated in Fig. 2a, showing how an increase of acceptor content in the blend leads to a larger share of volumes where excitons do not dissociate effectively, thereby increasing the recombination (measured as photoluminescence) and lowering the dissociation (measured as generated current).

In this work, we use two high-performing binary organic absorber systems: the donor polymer D18[36] mixed with the non-fullerene acceptor Y6[37] enabling record-breaking efficiencies in the field of organic photovoltaics[36,38] and the donor polymer PM6[39,40] mixed with DTY6,[41] a Y6 derivative featuring long branched alkyl chains to improve solubility and enable processing from non-chlorinated solvents. The chemical compositions are shown in Fig. 2b and c and the full names of the materials are provided in section 1 of the SI.

To assess the impact of increased NFA content on generated current density, organic solar cells were fabricated as illustrated in Fig. 1a (right side). The architecture comprises a transparent hole contact consisting of Indium Tin Oxide (ITO) and PEDOT:PSS. The electron contact features a PDIN layer with
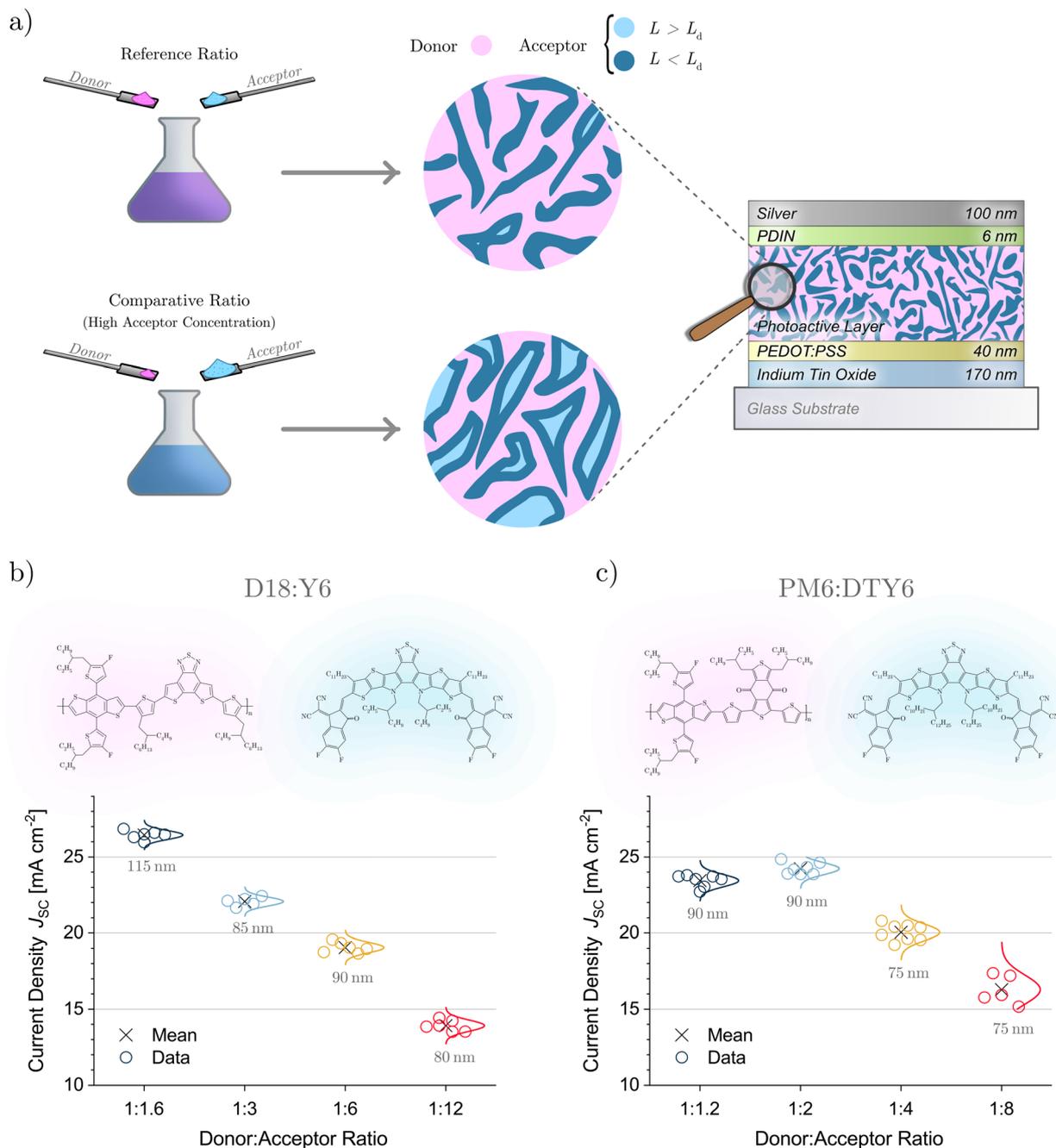

Fig. 2 (a) Schematic illustration of the organic solar cell architecture (right) and the morphological evolution of the bulk heterojunction (middle) with increasing acceptor content. The acceptor domains are visualized as regions within the exciton diffusion length that enable efficient exciton dissociation (dark blue) and regions beyond the diffusion length where exciton recombination is more likely (light blue). (b and c) Chemical structures of the donor and acceptor materials, together with the short-circuit current density as a function of the donor–acceptor weight ratio for D18:Y6 and PM6:DTY6, respectively. The corresponding photoactive-layer thicknesses are indicated below each J_{SC} distribution. The distribution functions illustrate the spread of the data and thus the associated experimental uncertainty.

silver on top. Detailed procedures for device fabrication are provided in section 2 of the SI.

Under the assumption that the charge collection efficiency η_{CC} is close to unity at 0 V the short circuit current density J_{SC} can be employed as a measure for J_{gen} $\left(J_{gen} = \dfrac{J(V)}{\eta_{CC}(V)} \approx J_{SC} \right)$. The evolution of J_{SC} as a function of $r_{D:A}$ is shown in Fig. 2b and c with the thickness of the photoactive layer denoted at each variation. For D18 : Y6 we observe a $J_{SC} = 26.5(3)$ mA cm^{-2} at the reference $r_{D:A} = 1 : 1.6$. As the acceptor fraction increases, J_{SC} decreases continuously, dropping by nearly 50% to 13.9(4) mA cm^{-2} at $r_{D:A} = 1{:}12$. For PM6:DTY6 the $J_{SC} = 23.5(4)$ mA cm^{-2} at the reference ratio $r_{D:A} = 1{:}1.2$ increases slightly when increasing the acceptor content to $r_{D:A} = 1{:}2$ before decreasing with the further increasing of acceptor content (down to 16.3(9) mA cm^{-2} at $r_{D:A} = 1{:}8$). However, as evident from the full set of photovoltaic performance parameters (see Section S3 of the SI), the power conversion efficiency for PM6 : DTY6 (and also D18:Y6) continuously decreases with each step of increased acceptor content, demonstrating that the reference ratio indeed shows the best performance. We also see a slight reduction in fill factor, however, not to a degree which would significantly alter η_{CC} at 0 V. Hence, the decrease in J_{SC} indicates a reduced charge generation yield as a result of the reduction in dissociation efficiency.
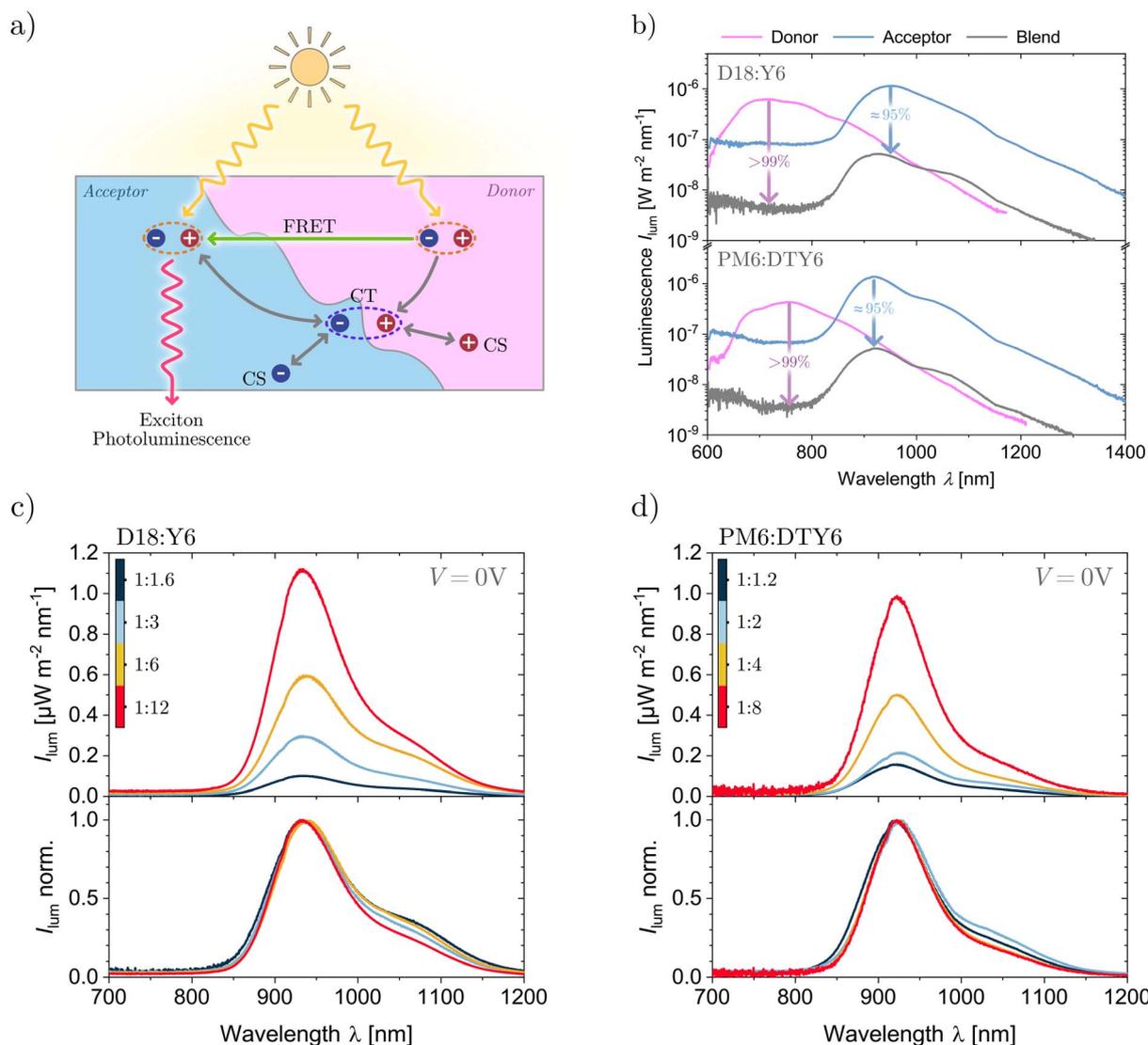

Fig. 3 (a) Schematic depiction of the PL emission in non-fullerene acceptor based organic solar cells. Excitons generated on the donor phase can either transfer to the charge-transfer (CT) state or to the acceptor exciton state via Förster resonance energy transfer (FRET). Excitons on the acceptor phase can dissociate into the CT state with a probability given by the exciton dissociation efficiency η_{ED}, or recombine with the radiative fraction given by the photoluminescence quantum yield (PLQY). Recombination of charge carriers via the acceptor exciton state is suppressed by measuring under short-circuit conditions. (b) PL spectra of films on glass substrates for pure donor (purple), pure acceptor (blue) and blend (gray) films with their respective reference donor:acceptor mixing ratio for D18 : Y6 (top) and PM6 : DTY6 (bottom). The donor exciton PL is quenched by >99% while the acceptor PL is quenched by ≈95%. (c) and (d): PL spectra of complete solar cells under short circuit condition for D18 : Y6 and PM6 : DTY6 as a function of the donor–acceptor mixing ratio, with the normalized PL spectra shown below.

3.2. Photoluminescence to probe non-dissociation of excitons

Photoluminescence spectroscopy provides a direct mean to probe the radiative recombination pathways in organic solar cells (see Section S4 in the SI for experimental details). Unlike in crystalline semiconductors, where PL mainly reflects band-to-band recombination, the emission in organic semiconductors originates from a combination of excitonic- and CT-recombination pathways. The relevant mechanisms are illustrated in Fig. 3a. Upon photoexcitation, excitons are generated on both the donor and the acceptor phases. Excitons on the donor can either diffuse to the interface and form CT complexes there or, due to overlap of the donor's emission spectrum and the acceptors absorption spectrum, transfer to the acceptor *via* Förster Resonance Energy Transfer (FRET), populating the acceptor exciton state.[18–22] Because of these efficient transfer processes, the donor emission is almost entirely suppressed, as confirmed by the PL spectra of pure donor *vs.* blend films shown in Fig. 3b, where the donor PL is reduced by more than 99%.

In contrast, excitons on the acceptor (either photo-excited or FRET transferred) dissociate less efficiently to separated charge carriers. This PL is quenched by roughly 95%, indicating that a small fraction of excitons recombine radiatively before reaching an interface. Consequently, the PL spectrum of the blend is dominated by emission from the acceptor excitons and can be described by a single photoluminescence quantum yield (PLQY) corresponding to that of the non-fullerene acceptor. This is a crucial factor for the proposed methodology. Given an interplay of donor and acceptor PLQY, an effective PLQY would need to be estimated and this would not cancel out in eqn (2) as changing the donor acceptor ratio would lead to an altering in PLQY as well.

While the majority of separated charge carriers recombine non-radiatively *via* the weakly emissive CT-state, a small fraction of charge carriers recombine also *via* the acceptor singlet state (S_1) emitting PL with this energy due to the small energetic offset between donor and acceptor HOMO levels.[42–44] This radiative channel contributes on the order of 10% to the overall PL signal under open circuit condition.[45,46] To isolate the PL associated with non-dissociated excitons, measurements are performed under short-circuit conditions, where the extraction of charge carriers suppresses their recombination. Although the exciton PL has been reported to be field-dependent for low-offset systems,[47–51] time-resolved PL studies in a previous work of ours have shown that its intensity changes by less than 4% between open- and short-circuit conditions for the same high-performance organic solar cells used in this study.[46] In that work, it was also shown that the PL of separated charge carriers in D18 : Y6 is supressed to <0.1% of the global PL already at 0.6 V. Thus, PL measurements under short-circuit conditions accurately reflect the recombination of photogenerated excitons and can be used as a direct measure for non-dissociated excitons.

The steady-state PL spectra of the solar cells at 0 V for varying donor : acceptor ratios are shown in Fig. 3c and d with the normalized spectra depicted in the bottom. For both absorber materials we see a strong increase in PL intensity with increasing acceptor content as expected from increased non-dissociation as a result of large acceptor domains.

At the same time, we see that the spectral shape is largely preserved, with a slight narrowing of the main (0–0) peak and a reduction in the 0–1 (adjacent shoulder peak at $\lambda_{0-1} \approx 1070$ nm) to 0–0 intensity ratio. These effects are congruent with higher molecular order.[52–54] Importantly, no additional donor-related emission emerges across the acceptor variation, confirming that donor exciton recombination remains negligible. Hence, donor excitons are still efficiently either directly dissociated at the interface or FRET transferred to the acceptor. Since FRET only redistributes excitons to the acceptor S_1 state (where they are treated equivalently to directly photo-generated acceptor excitons in our analysis) possible variations in FRET efficiency with acceptor content are inherently accounted for in the analysis. The emission can therefore still be described by a single PLQY across the composition variation.

Having established that the PL shape remains unchanged, we now consider the experimental uncertainty associated with the PL intensity. Measurements of multiple similar probes have shown that the PL variation between samples constitutes the largest contribution to the error on this quantity (∼10%). List *et al.* have shown that this PL variation mainly arises from thickness variations of the photoactive layer (here ±10 nm) and thereby variation in outcoupling efficiencies due to thin film interference effects.[55] Hence, this error is also larger than the error expected from field-dependent exciton PL quenching for the systems studied.

3.3. Quantifying the change in exciton photogeneration from absorptance measurements

The final quantity required for determining the exciton dissociation efficiency is the change in generation of photogenerated excitons g_{PE} as stated in eqn (5). To do so, the absorptance of the photoactive layer in the reference case $A_{PAL}(\lambda)$ and the comparative case $A'_{PAL}(\lambda)$ is needed. However, the global absorptance of the device stack as obtained from reflectance and transmittance measurements contains both the absorptance of the photoactive layer and other parasitic absorption. It can therefore be expressed as

$$A(\lambda) = A_{PAL}(\lambda) + A_{par}(\lambda) \tag{8}$$

where A_{par} denotes the parasitic absorption in the layers of the device stack that do not lead to exciton generation (such as the glass substrate and interlayers). Note that A_{par} does not cancel out in the calculation of g_{PE} due to it being inside the integral. Hence, to obtain $A_{PAL}(\lambda)$ isolated, it is necessary to either conduct optical simulations or carry out approximations on the global absorptance measurements. Both options and their feasibility will be demonstrated and discussed in the following.

First, the option of optical simulation is demonstrated. To do so, the refractive index (n) and extinction coefficient (k) of each individual layer were determined from reflectance and transmittance measurements, and the layer thicknesses were obtained from profilometry (see Section S5 in the SI for fitting

details and Fig. 6a for the n and k values). Using these optical constants and thicknesses, the absorptance of the photoactive layer within the layer stack could be estimated. The results are depicted as dashed lines in Fig. 4a and b. In both material systems, the absorptance decreases in the short-wavelength region (where the donor primarily absorbs) while remaining nearly constant in the long-wavelength region, which is dominated by acceptor absorption.[41] This behavior is consistent with the expected optical response when increasing the acceptor content in the blend.

Using the spectral photonflux of the solar simulator which closely resembles the AM1.5 G spectrum (depicted in Fig. 4c), g_{PE} can now be directly calculated. The results are shown in Fig. 4d (red lines with symbols). For D18 : Y6, g_{PE} decreases continuously with increasing acceptor content, reaching roughly 85% of its initial value at $r_{D:A} = 1:12$. For PM6 : DTY6, g_{PE} increases slightly at $r_{D:A} = 1:2$, before also decreasing to about 85% at $r_{D:A} = 1:8$. The error on g_{PE} (3%) arises from layer thickness uncertainties in the simulation.

While optical simulations yield accurate values for the photoactive-layer absorptance within the layer stack taking into account both parasitic absorptances and interference effects, they are comparatively tedious to obtain and prone to systematic uncertainties originating from optical fitting procedures. To circumvent this effort, we demonstrate a more pragmatic approach to approximate g_{PE} directly from the measured global absorptance and evaluate its feasibility for the presented method. The absorptance spectra of the full stacks are depicted in Fig. 4a and b as solid lines. The difference between the simulated photoactive-layer absorptance and the full-stack absorptance is illustrated as the shaded area, representing parasitic absorption. One part of the parasitic absorptance arises from transparent electrode absorptance, $A_{TE}(\lambda)$, consisting of glass/ITO/PEDOT:PSS. This stack exhibits increased absorption below 400 nm and contributes significantly below the acceptor band gap (>920 nm) as also shown in Fig. 4a and b. First order correcting for this parasitic absorptance, the absorptance of the photoactive layer can be approximated by
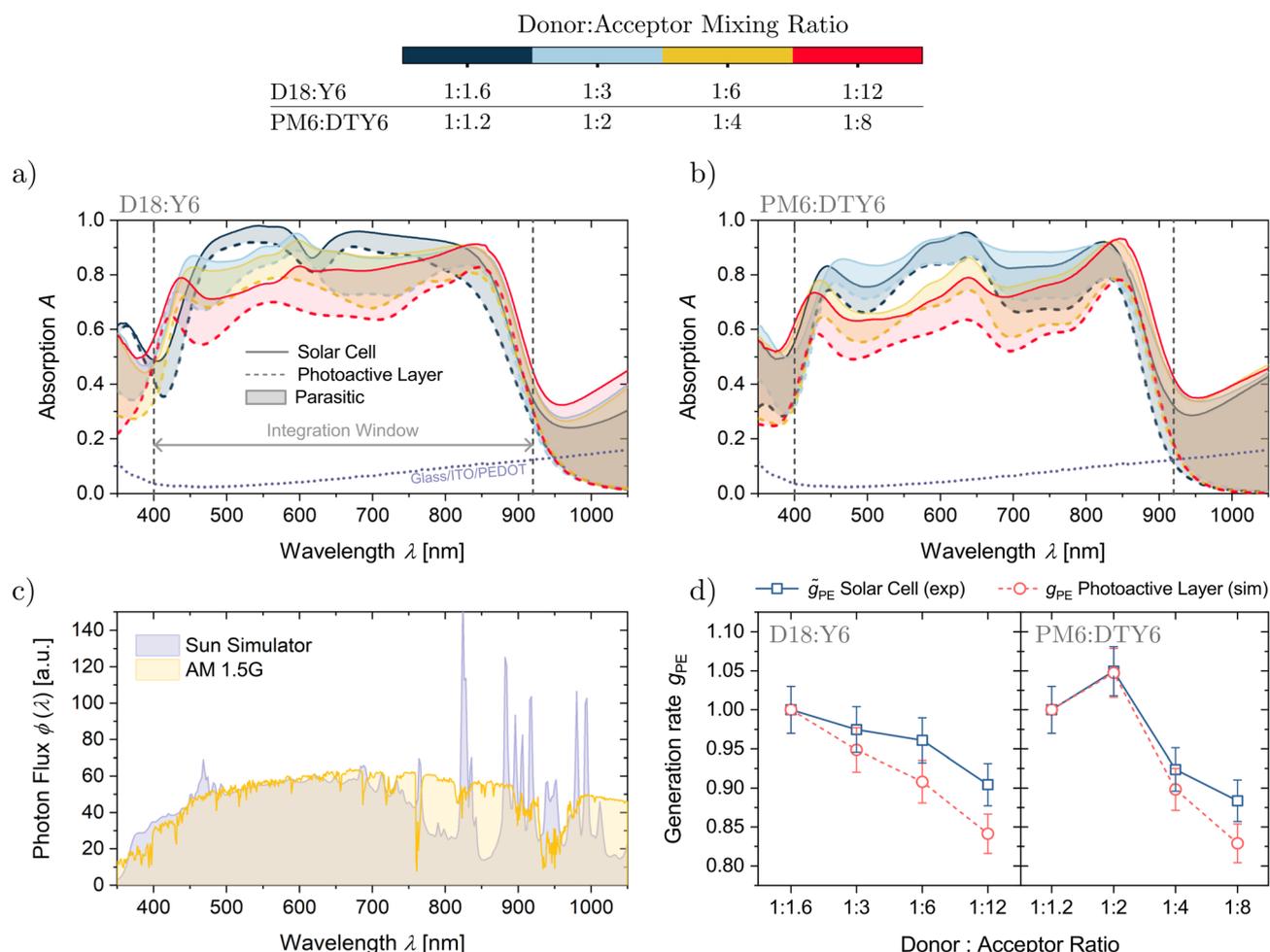

Fig. 4 (a and b) Absorptance of the full-stack solar cell devices (solid lines) and the optically simulated photoactive-layer absorptance within the stack (dashed lines) as a function of the donor–acceptor mixing ratio for D18 : Y6 and PM6 : DTY6. The parasitic absorption in the layer stack is indicated by the shaded regions. The absorptance of the glass/ITO/PEDOT substrate stack is shown as a dotted line. (c) Photon flux of the solar simulator used in this work (purple), compared to the AM1.5 G reference spectrum (yellow). (d) Relative integrated exciton generation calculated from the simulated photoactive-layer absorptance (red) and from first-order correction of the measured full-stack absorptance (blue).

subtracting the first optical pass through this stack and also account for the second optical pass. The latter can be expressed as the product of the reflectance $R(\lambda)$ with A_{TE}. However, since the reflected light intensity of the full device stack is measured after having been transmitted again through the transparent electrode, it needs to be weighted by $(1 - A_{TE})$. Furthermore, since transmittance T is zero for opaque devices $R(\lambda)$ can be expressed as $1 - A(\lambda)$. With these considerations, the approximated absorptance of the photoactive layer $\tilde{A}_{PAL}(\lambda)$ can be expressed as

$$\tilde{A}_{PAL}(\lambda) \approx A(\lambda) - \underbrace{A_{TE}(\lambda)}_{\text{1st optical pass}} - \underbrace{\frac{1 - A(\lambda)}{1 - A_{TE}(\lambda)}A_{TE}(\lambda)}_{\text{2nd optical pass}}$$

$$- \ldots (\text{higher-order passes neglected}) \qquad (9)$$

We can then use this approximated $\tilde{A}_{PAL}(\lambda)$ in eqn (5) and restrict the integration window to the spectral region where the bulk of absorption occurs (400 nm to 920 nm) to obtain an approximated change in generation rate, denoted as $\tilde{g}_{PE}$. The results for this approximation are shown in Fig. 4d as blue lines with symbols. For both material systems, $\tilde{g}_{PE}$ follows the trend of g_{PE} determined from simulated layer absorption.

Towards higher acceptor concentrations, however, the approximated $\tilde{g}_{PE}$ slightly overestimates g_{PE} determined from simulated layer absorption with the highest deviations being at 7% and thus larger than the statistical error. This discrepancy arises because, as the absorptance of the photoactive layer decreases, the relative contribution of parasitic absorption (particularly from layers not included in the correction accounting for the transparent-electrode) becomes more significant. In addition, this effect is amplified with reduced photoactive layer absorptance as a larger fraction of unabsorbed light is reflected and transmitted through the device stack a second time, further enhancing parasitic absorption in the non-active layers. Together, these effects lead to an underestimation of the actual reduction in the photoactive-layer absorptance.

This systematic error in the presented approximation approach could therefore be further reduced by employing interlayers with even less parasitic absorption. Also, given that the net absorptance of the photoactive layers would remain rather constant for the comparative devices, the amplification effect of increased parasitic absorption would also be further suppressed, reducing this systematic error.

Despite these effects, the deviation between the two methods remains minor, supporting the validity of the approximation approach. In the following analysis of the exciton dissociation efficiency, we will demonstrate the feasibility of the pragmatic approach using the approximated $\tilde{g}_{PE}$. To accurately reflect the uncertainty of this approximation, the uncertainty on $\tilde{g}_{PE}$ will be taken as the larger of either the statistical absorptance measurement error (3%) or the systematic error arising from its difference to the simulated layer absorptance. We will also compare the resulting values of η_{ED} to those obtained using the g_{PE} obtained from photoactive layer absorptance simulation,

highlighting the differences in precision and the robustness of the approximation.

3.4. Calculation of exciton dissociation efficiency

In this section, we demonstrate the calculation of the exciton dissociation efficiency employing the pragmatic absorptance approximation approach while showing the results with the precise simulated layer absorptance values in Section S6 in the SI.

The values for j_{gen}, $i_{lum,PE}$, and $\tilde{g}_{PE}$ are depicted in Fig. 5a. Using the framework derived in Section 2, specifically eqn (6) and (7), the exciton dissociation efficiencies of the reference device, η_{ED}, and of the comparative devices with modified blend ratios η'_{ED}, can be calculated. The resulting values are shown in Fig. 5b, where the reference device is indicated in purple and the comparative devices in green. Error bars are determined via Gaussian error propagation considering symmetric errors (see Section S7 in the SI).

The extracted η_{ED} values, obtained independently from each donor–acceptor variation, are in excellent agreement with one another. This consistency demonstrates both the robustness of the method and its applicability across arbitrary comparative blend ratios. In particular, the results strongly support the underlying assumptions of composition-independent η_{CS} and η_{CC} at 0 V, as well as an approximately constant PLQY across the studied compositions. The close agreement between independently extracted values indicates that possible deviations from these assumptions remain small within the present analysis, yielding stable and reproducible η_{ED} values. Also η'_{ED} can be obtained for each comparative device and decreases continuously with increasing acceptor fraction, in line with the expected increase in acceptor-rich domains that do not contribute to exciton dissociation.

Particular attention should be paid to the behavior of the uncertainties. While the error of η'_{ED} remains large toward high acceptor concentrations, the uncertainty in η_{ED} is actually minimized when using comparative devices with the highest acceptor content, even though the individual uncertainties in j_{gen} and especially $\tilde{g}_{PE}$ are larger in this regime. The underlying reason is that the exciton PL intensity increases by a factor of 5–10 at the highest acceptor concentrations shown here, meaning the fraction of non-dissociated excitons, $(1 - \eta_{ED})$, normalized by the generation rate, increases by the same factor from reference to the comparative device. For reference devices with high dissociation efficiencies close to unity, this strongly narrows the allowable range of $(1 - \eta_{ED})$ and therefore reduces the error on η_{ED} to 1% for D18 : Y6 and 1.6% for PM6 : DTY6, respectively.

In contrast, when the relative changes are small (even given the lower individual uncertainties), the error on the exciton dissociation efficiencies is large. This can be clearly observed for PM6 : DTY6 when the comparative device has only a moderately increased acceptor content ($r_{D:A} = 1{:}2$). In that case, the quantities j_{gen} and g_{PE} show very small changes (and can be considered nearly constant within their uncertainty), while the PL increases by only about 30%. Consequently, the constraint
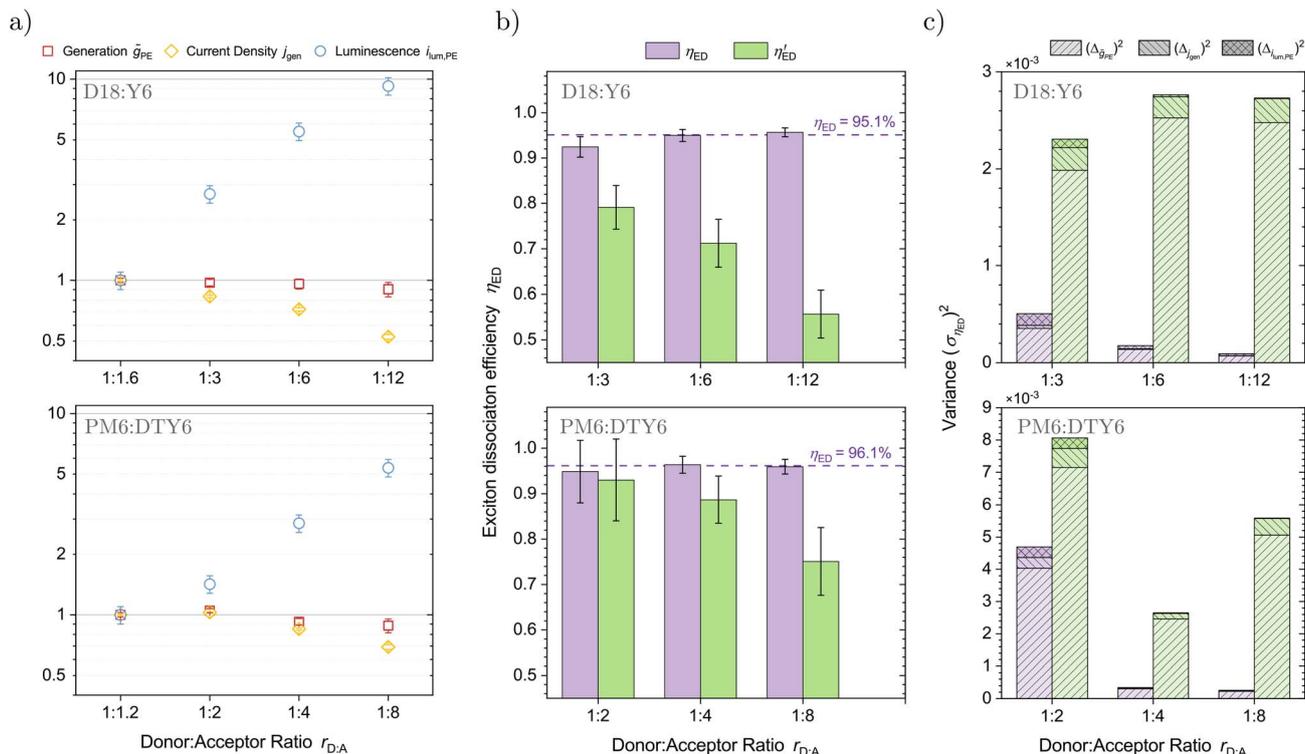
Fig. 5 Results for D18 : Y6 (top row) and PM6 : DTY6 (bottom row). (a) Evolution of the normalized quantities: integrated photogeneration of excitons g_{PE} (red), generated current density j_{gen} (yellow), and exciton photoluminescence $i_{lum,PE}$ (blue) as a function of the donor−acceptor ratio. (b) Exciton dissociation efficiencies of the reference devices (η_{ED}, purple) and the comparative devices (η'_{ED}, green), with the weighted mean shown as a dashed line. (c) Variance analysis of the values shown in (b), with the contributing uncertainty components from g_{PE}, j_{gen}, and $i_{lum,PE}$ encoded in the stacked bars.

on $(1 - \eta_{ED})$ is much weaker, and the uncertainties of both dissociation efficiencies remain comparatively large (4% to 5%).

A closer inspection of the error bars is provided in Fig. 5c, where the variance (*i.e.*, squared uncertainty) of each value in Fig. 5b is plotted. The bars are subdivided into the individual variance contributions of each input variable (see Section S7 in the SI for details). It becomes evident that while the overall variance of η_{ED} decreases toward higher acceptor concentrations, the variance of η'_{ED} remains comparatively large. At the same time, the photogeneration term $\tilde{g}_{PE}$ increasingly dominates the total variance for both quantities, whereas the contributions from j_{gen} and $i_{lum,PE}$ are comparably low and nearly negligible with the measurement uncertainties considered here. Importantly, even though the uncertainty in $\tilde{g}_{PE}$ is largest at highest acceptor concentrations presented here (where its systematic component becomes significant) the total variance of η_{ED} is still minimized in this regime.

Since the accuracy of each extracted η_{ED} value is reflected in its individual uncertainty, a weighted mean can be calculated using inverse-variance weighting (see Section S8 in the SI). This yields $(95.1 \pm 0.7)\%$ for D18 : Y6 and $(96.1 \pm 1.2)\%$ for PM6 : DTY6.

A crucial aspect for interpreting the results is the technically asymmetric nature of the global uncertainty. Since the uncertainty in $\tilde{g}_{PE}$ becomes dominated by its systematic component at high acceptor concentrations, the resulting error on the

weighted mean is not symmetric but reflects the uncertainty in the positive direction. This arises because $\tilde{g}_{PE}$ underestimates the true reduction in relative generation rate, which in turn leads to a modest underestimation of η_{ED}. Hence, the uncertainty in the negative direction is overestimated here meaning that the actual dissociation efficiency is likely equal or higher than the value reported.

To obtain more precise results without systematic uncertainty, η_{ED} can be evaluated using g_{PE} obtained from simulated photoactive-layer absorptance. The results of this analysis are provided in Section S6 of the SI. There, we obtain $(96.2 \pm 0.4)\%$ for D18 : Y6 and $(97.2 \pm 0.6)\%$ for PM6 : DTY6. Both values are approximately 1% higher than those obtained with the absorptance approximation, confirming that the $\tilde{g}_{PE}$ approximation is feasible but introduces a slight systematic underestimation. With the simulated absorptance, the uncertainty is reduced further by roughly a factor of two, reaching the 0.5% range.

These results demonstrate the robustness and high precision of the comparative framework for the investigated high-offset systems, where exciton dissociation is largely field-independent. In the present work, η_{ED} is evaluated at 0 V. For low-offset systems, in which exciton dissociation can exhibit a pronounced field dependence, the methodology can in principle be extended by evaluating η_{ED} at multiple applied bias voltages, thereby yielding $\eta_{ED}(V)$. In such cases, it would also be

necessary to verify that charge separation and collection efficiencies remain morphology-independent across the compared blend ratios. This could again be assessed within the framework by evaluating multiple comparative ratios at a given bias and examining the consistency of the independently extracted $\eta_{ED}(V)$ values. Systematic morphology-dependent variations in charge separation or collection would manifest as inconsistencies exceeding the expected experimental uncertainty.

3.5. Comparison with internal quantum efficiency from optical simulations

In the following, we compare the exciton dissociation efficiencies obtained with the proposed method to values conventionally extracted by explicitly solving eqn (1) for η_{ED} at the reference morphology. For this purpose, eqn (1) can be rearranged as

$$\eta_{ED} = \frac{J(V)}{\eta_{CC}(V)\eta_{CS}J_{gen,PE}} \quad (10)$$

where $J(V) = \eta_{CC}(V)J_{gen}$ represents the collected current density at the electrodes and $J_{gen,PE} = q\int_0^\infty A_{PAL}(\lambda)\Phi_{ph}(\lambda)d\lambda$ describes the current density of photogenerated excitons. In contrast to the donor–acceptor variation approach, η_{CS} and η_{CC} do not cancel out in this expression and thus must be explicitly approximated. Here, we evaluate eqn (10) at short-circuit conditions ($V = 0$), where $\eta_{CC} \approx 1$ is a valid assumption. The charge separation efficiency η_{CS} describes the probability that CT states dissociate into separated charge carriers and can be estimated from the ratio of dissociation to recombination rates.[17,56] While η_{CS} can be limiting in low-offset OSCs,[57] the systems investigated here exhibit sufficiently large energetic offsets, such that $\eta_{CS} \approx 1$ is also reasonable.
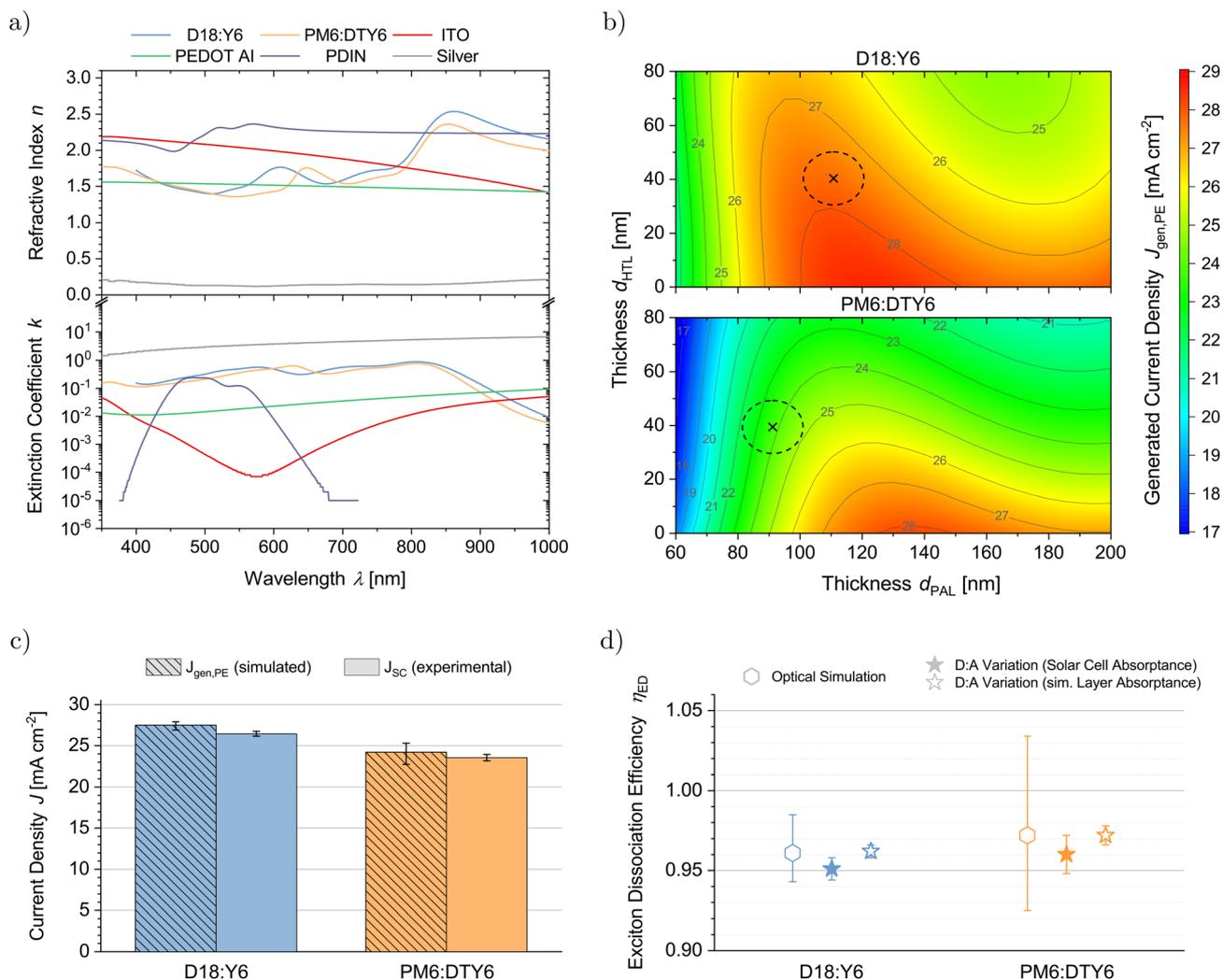

Fig. 6 (a) Refractive index (top) and extinction coefficient (bottom) spectra for the materials used in the solar cell device stacks. (b) Simulated current density heat maps showing the dependence on both HTL thickness and PAL thickness for D18 : Y6 (top) and PM6 : DTY6 (bottom). Measured thicknesses are indicated by a cross, with dashed circles representing the associated uncertainties. (c) Generated current density J_{gen} from optical simulation (hatched bars), with errors based on thickness variation, and experimentally determined J_{gen} (solid bars), with error bars representing the standard error of the mean. (d) Exciton dissociation efficiency η_{ED} derived from the optical simulation approach (diamonds), compared to η_{ED} values obtained using the donor : acceptor variation method.

Table 1 Exciton dissociation efficiency results

Method	D18 : Y6	PM6 : DTY6
Conventional optical simulation		
η_{ED} [%]	$96.1\,^{+2.4}_{-1.8}$	$97.2\,^{+6.2}_{-4.7}$
Donor : Acceptor variation		
η_{ED} [%] (using approximated absorptance from solar cell)	95.1 ± 0.7	96.1 ± 1.2
η_{ED} [%] (using simulated layer absorptance)	96.2 ± 0.4	97.2 ± 0.6

The remaining quantity required is $J_{\text{gen,PE}}$, which we determine by optical simulation of the photoactive-layer absorptance inside the full device stack (analogous to Section 3.3). The refractive index (n) and extinction coefficient (k) of each layer were extracted from reflectance and transmittance measurements and are shown in Fig. 6a. These optical constants were then used in a transfer-matrix simulation to obtain $A_{\text{PAL}}(\lambda)$, which, combined with the AM1.5 G photon flux $\Phi_{\text{ph}}(\lambda)$, yields $J_{\text{gen,PE}}$.

The calculated $J_{\text{gen,PE}}$ values show a strong dependence on the active-layer thickness d_{PAL} and also on the PEDOT:PSS thickness d_{HTL}, as evident from the heat map depicted in Fig. 6b. The cross markers indicate the measured mean thicknesses for each solar cell with the dashed circle representing the uncertainty (± 10 nm). The resulting values of $J_{\text{gen,PE}}$ are $27.5\,^{+0.4}_{-0.6}$ for D18 : Y6 and $24.2\,^{+1.1}_{-1.5}$ for PM6 : DTY6, as also depicted in Fig. 6c as hatched bars, where asymmetric error bars reflect the non-linear dependence on layer thickness variations. Depicted as plain bars are also the J_{SC} values representing the approximation for the generated current density (26.5 ± 0.3 and 23.5 ± 0.4, respectively). The error bars here represent the standard error on the mean value.

Dividing the measured short-circuit current by the simulated photogenerated current directly yields the conventional approximation of the exciton dissociation efficiency. The results are shown in Fig. 6d as open hexagons. Uncertainties were calculated using standard Gaussian error propagation, incorporating the asymmetric uncertainty of $J_{\text{gen,PE}}$ and the standard error on the mean of J_{SC} (details in Section S9 of the SI). For comparison, the exciton dissociation efficiencies obtained from the novel donor–acceptor variation approach are included as star symbols, once for the absorptance approximation approach (closed stars) and the simulated layer absorptance approach (open stars). The corresponding values are summarized in Table 1.

Both approaches yield values that agree within their respective uncertainties, despite relying on different methodologies. This confirms the validity of the donor–acceptor variation approach while simultaneously indicating that the assumptions made in the method based on conventional optical simulation are reasonable. There is, however, a significant difference in the uncertainty range. Even though the conventional optical simulation approach only accounts for uncertainties in the layer thickness measurements (± 10 nm) and the standard error of J_{SC}, the resulting error in η_{ED} remains significant: approximately 2% to 3% for D18 : Y6 and up to 5%

for PM6 : DTY6. In the latter case, the upper bound even exceeds $\eta_{\text{ED}} = 1$, placing the value outside the physically valid range. Moreover, these uncertainty estimates do not include potential systematic errors arising from the optical simulation itself or from the precision of the active area used for determining J_{SC}. In addition, the assumptions $\eta_{\text{CS}} \approx 1$ and $\eta_{\text{CC}} \approx 1$ are not considered in the uncertainty analysis.

In contrast, the donor–acceptor variation method—already with the approximated absorptance—yields uncertainties around 1% without requiring optical modeling or assumptions about charge separation or collection and despite considering a generous uncertainty for the absorptance estimate. When using more accurate absorptance values (from optical simulation), the uncertainty can be even further reduced to roughly 0.5%, also eliminating the slight systematic underestimation of η_{ED}.

Overall, this illustrates that the proposed novel method with the comparative approach provides a more robust and precise determination of the exciton dissociation efficiency, particularly for high-performance morphologies with η_{ED} close to 100%.

4. Conclusion

In this work, we presented a generally applicable framework to determine the exciton dissociation efficiency η_{ED} in non-fullerene acceptor based organic solar cells, relying solely on the relative change of photoluminescence, short-circuit current, and absorptance of the photoactive layers between two blend morphologies, that is, the reference device and a comparative device with intentionally reduced exciton dissociation efficiency. The latter was achieved by increasing the acceptor fraction in the blend to form larger acceptor domains, thereby increasing the volume where excitons are more likely to recombine before reaching a donor–acceptor interface.

With this comparative approach, many prefactors associated with detection, emission, and device geometry cancel out. Furthermore, explicit numeric assumptions on charge separation and charge collection efficiencies are not needed. As a result, the method directly yields η_{ED} for both the reference and comparative devices. The approach was demonstrated on the high-performing systems D18 : Y6 and PM6 : DTY6. Across multiple blend ratios, the extracted reference exciton dissociation efficiencies showed excellent consistency, yielding $\eta_{\text{ED}} = 96.2 \pm 0.4\%$ for D18 : Y6 and $97.2 \pm 0.6\%$ for PM6 : DTY6. We also demonstrated that a pragmatic photoactive-layer absorptance approximation approach without any optical simulation

can also be employed to obtain robust lower bounds for the exciton dissociation efficiency (here: 95.1 ± 0.7% and 96.1 ± 1.2%, respectively).

These results were then compared to conventional optical simulation based IQE estimates, confirming the physical accuracy of the proposed method. Although both approaches yield results that agree within their respective uncertainties, the simulation-based method suffers from substantially larger uncertainty (3% to 5% absolute) due to its sensitivity to layer thicknesses and its reliance on assumptions such as $\eta_{CS} \approx 1$ and $\eta_{CC} \approx 1$. In contrast, our method remains highly precise with an absolute uncertainty of only ~0.5%.

The key strength of the proposed method lies in its self-normalizing character and the dual constraints it imposes: the change in J_{SC} relative to the change in exciton generation directly reflects the change in η_{ED}, while the PL signal — likewise normalized to the change in generation — constrains the non-dissociated exciton fraction $(1 - \eta_{ED})$, preventing unphysical values above 100%. Furthermore, absorptance measurements used for the change in generation inherently account for variations in active-layer thickness, hence the method enables robust determination of η_{ED} without the need for absolute calibrations or thickness matching between these devices.

Overall, the proposed approach offers a precise and experimentally accessible route to quantify exciton dissociation efficiency in state-of-the-art organic solar cells, particularly when this quantity approaches unity and conventional methods lose accuracy. We anticipate that this methodology will be valuable for investigating exciton dissociation in low-offset systems and for facilitating targeted morphology optimization, thereby supporting the design of next-generation high-performance organic solar cells through reliable identification of dissociation-related loss channels.

Author contributions

Conceptualization: J. F., M. L., R. P. Methodology: J. F. Data curation: J. F. Formal analysis: J. F., M. L. Investigation: J. F., L. P. Writing: J. F. Visualization: J. F. Review: M. L., R. P., A. B., U. W. Project administration: A. B., U. W.

Conflicts of interest

The authors declare no competing interests.

Data availability

The datasets generated in this study are available upon reasonable request.

Supplementary information (SI) is available. See DOI: https://doi.org/10.1039/d6el00011h.

Acknowledgements

References

1 D. Xie, B. Wu, Q. Wu, B. Deng, J. Li, Z. Chen, J. Zhu, R. Xia, L. Pan, K. Liu, *et al.*, Scalable polymer for large-area semitransparent organic photovoltaics, *Joule*, 2025, **9**(11), 102173.

2 Z. Zheng, J. Wang, P. Bi, J. Ren, Y. Wang, Y. Yang, X. Liu, S. Zhang and J. Hou, Tandem organic solar cell with 20.2% efficiency, *Joule*, 2022, **6**, 171.

3 Y. Sun, L. Wang, C. Guo, J. Xiao, C. Liu, C. Chen, W. Xia, Z. Gan, J. Cheng, J. Zhou, *et al.*, π-extended nonfullerene acceptor for compressed molecular packing in organic solar cells to achieve over 20% efficiency, *J. Am. Chem. Soc.*, 2024, **146**, 12011.

4 J. Qin, Q. Xi, N. Wu, B. Liu, C. Yue, J. Fang, Z. Wang, Y. Du, Q. Zhang, Z. Wang, *et al.*, Improved damp heat and thermal cycling stability of organic solar cells, *Nat. Energy*, 2025, **10**(12), 1439–1449.

5 E. K. Solak and E. Irmak, Advances in organic photovoltaic cells: a comprehensive review of materials, technologies, and performance, *RSC Adv.*, 2023, **13**, 12244.

6 K. Fukuda, K. Yu and T. Someya, The future of flexible organic solar cells, *Adv. Energy Mater.*, 2020, **10**, 2000765.

7 L. Pap, M. List, R. Haberstroh, L. Bienkowski, M. Mattenheimer, T. Kroyer, J. Faisst, B. Zimmermann and U. Würfel, Metal-less top electrode semitransparent organic solar modules with an average visible transmission of 51% and a light utilization efficiency of 4%, *Advanced Science*, 2025, e07521.

8 Y. Li, X. Huang, H. K. Sheriff Jr and S. R. Forrest, Semitransparent organic photovoltaics for building-integrated photovoltaic applications, *Nat. Rev. Mater.*, 2023, **8**, 186.

9 J. Ding, H. Mou, H. Chen, J. Xu, W. Sun, J. Zhu, Y. Wang, Y. Huang, Y. Li and Y. Li, Manipulating molecular stacking for semitransparent organic photovoltaics achieving light utilization efficiency> 6%, *Adv. Mater.*, 2025, 2420439.

10 Y.-F. Zhang, W.-S. Chen, J.-D. Chen, H. Ren, H.-Y. Hou, S. Tian, H.-R. Ge, H.-H. Ling, J.-L. Zhang, H. Mao, *et al.*, Optically enhanced semitransparent organic solar cells with light utilization efficiency surpassing 5.5%, *Adv. Energy Mater.*, 2024, **14**, 2400970.

11 L. J. A. Koster, S. E. Shaheen and J. C. Hummelen, Pathways to a new efficiency regime for organic solar cells, *Adv. Energy Mater.*, 2012, **2**, 1246.

12 M. Samiee, S. Konduri, B. Ganapathy, R. Kottokkaran, H. A. Abbas, A. Kitahara, P. Joshi, L. Zhang, M. Noack and V. Dalal, Defect density and dielectric constant in perovskite solar cells, *Appl. Phys. Lett.*, 2014, **105**, 153502.

13 W. Dunlap Jr and R. Watters, Direct measurement of the dielectric constants of silicon and germanium, *Phys. Rev.*, 1953, **92**, 1396.

14 J. Blakemore, Semiconducting and other major properties of gallium arsenide, *J. Appl. Phys.*, 1982, **53**, R123.

15 S. Karuthedath, J. Gorenflot, Y. Firdaus, N. Chaturvedi, C. S. De Castro, G. T. Harrison, J. I. Khan, A. Markina, A. H. Balawi, T. A. D. Peña, *et al.*, Intrinsic efficiency limits in low-bandgap non-fullerene acceptor organic solar cells, *Nat. Mater.*, 2021, **20**, 378.

16 J. Bertrandie, J. Han, C. S. De Castro, E. Yengel, J. Gorenflot, T. Anthopoulos, F. Laquai, A. Sharma and D. Baran, The energy level conundrum of organic semiconductors in solar cells, *Adv. Mater.*, 2022, **34**, 2202575.

17 D. B. Riley, P. Meredith, A. Armin and O. J. Sandberg, Role of exciton diffusion and lifetime in organic solar cells with a low energy offset, *J. Phys. Chem. Lett.*, 2022, **13**, 4402.

18 K. Feron, W. J. Belcher, C. J. Fell and P. C. Dastoor, Organic solar cells: understanding the role of förster resonance energy transfer, *Int. J. Mol. Sci.*, 2012, **13**, 17019.

19 A. A. Mohapatra, V. Tiwari and S. Patil, Energy transfer in ternary blend organic solar cells: recent insights and future directions, *Energy Environ. Sci.*, 2021, **14**, 302.

20 M. Zhou, K. Zhang, X. Li, Y. Ge, W. Zhang, P. Lu and X. Hao, Improved exciton diffusion through modulating förster resonance energy transfer for efficient organic solar cells, *Sol. RRL*, 2024, **8**, 2400136.

21 B. R. Gautam, R. Younts, J. Carpenter, H. Ade and K. Gundogdu, The role of fret in non-fullerene organic solar cells: implications for molecular design, *J. Phys. Chem.*, 2018, **122**, 3764.

22 Y. Ouyang, R. Wang, X. Wang, M. Xiao and C. Zhang, Ultrafast energy transfer beyond the förster approximation in organic photovoltaic blends with non-fullerene acceptors, *Sci. Adv.*, 2025, **11**, eadr5973.

23 K. Nakano, K. Terado, Y. Kaji, H. Yoshida and K. Tajima, Reduction of electric current loss by aggregation-induced molecular alignment of a non-fullerene acceptor in organic photovoltaics, *ACS Appl. Mater. Interfaces*, 2021, **13**, 60299.

24 D. Hu, H. Tang, C. Chen, P. Huang, Z. Shen, H. Li, H. Liu, C. E. Petoukhoff, J. P. Jurado, Y. Luo, *et al.*, Insights into preaggregation control of y-series nonfullerene acceptors in liquid state for highly efficient binary organic solar cells, *Adv. Mater.*, 2024, **36**, 2402833.

25 W. Liu, R. Zhang, Q. Wei, C. Zhu, J. Yuan, F. Gao and Y. Zou, Manipulating molecular aggregation and crystalline behavior of a-da'd-a type acceptors by side chain engineering in organic solar cells: Photovoltaics: Special issue dedicated to professor yongfang li, *Aggregate*, 2022, **3**, e183.

26 D. Li, X. Zhang, D. Liu and T. Wang, Aggregation of non-fullerene acceptors in organic solar cells, *J. Mater. Chem. A*, 2020, **8**, 15607.

27 E. Feng, C. Zhang, J. Chang, F. Zhao, B. Hu, Y. Han, M. Sha, H. Li, X.-J. Du, C. Long, *et al.*, Constraining the excessive aggregation of non-fullerene acceptor molecules enables organic solar modules with the efficiency> 16%, *ACS Nano*, 2024, **18**, 28026.

28 S. A. Dowland, M. Salvador, J. D. Perea, N. Gasparini, S. Langner, S. Rajoelson, H. H. Ramanitra, B. D. Lindner, A. Osvet, C. J. Brabec, *et al.*, Suppression of thermally induced fullerene aggregation in polyfullerene-based multiacceptor organic solar cells, *ACS Appl. Mater. Interfaces*, 2017, **9**, 10971.

29 J. Yu, S. Li, M. Shi, H. Zhu and H. Chen, Recent advances in thermo-and photostabilities of organic solar cells: Material design and morphology control, *Polym. Sci. Technol.*, 2025, 25–45.

30 W. Li, Z. Xiao, J. Cai, J. A. Smith, E. L. Spooner, R. C. Kilbride, O. S. Game, X. Meng, D. Li, H. Zhang, *et al.*, Correlating the electron-donating core structure with morphology and performance of carbonoxygen-bridged ladder-type non-fullerene acceptor based organic solar cells, *Nano Energy*, 2019, **61**, 318.

31 Y. Xie, L. Ye, Y. Cai, X. Zhang, J. Xu, T. Wang, F. Liu and Y. Sun, Fine-tuning aggregation of nonfullerene acceptor enables high-efficiency organic solar cells, *Small Struct.*, 2021, **2**, 2100055.

32 J. Xue, H. B. Naveed, H. Zhao, B. Lin, Y. Wang, Q. Zhu, B. Wu, Z. Bi, X. Zhou, C. Zhao, *et al.*, Kinetic processes of phase separation and aggregation behaviors in slot-die processed high efficiency y6-based organic solar cells, *J. Mater. Chem. A*, 2022, **10**, 13439.

33 K. An, W. Zhong, F. Peng, W. Deng, Y. Shang, H. Quan, H. Qiu, C. Wang, F. Liu, H. Wu, *et al.*, Mastering morphology of non-fullerene acceptors towards long-term stable organic solar cells, *Nat. Commun.*, 2023, **14**, 2688.

34 J. Faisst, R. Patterson, M. List, L. Pap, Y. Thomann, D. Müller, S. W. Glunz, A. W. Bett and U. Würfel, Exciton dissociation efficiency in organic solar cells quantified via thermally induced acceptor aggregation and photoluminescence analysis, *Adv. Energy Mater.*, 2025, e03954.

35 G. Li, R. Zhu and Y. Yang, Polymer solar cells, *Nat. Photonics*, 2012, **6**, 153.

36 Q. Liu, Y. Jiang, K. Jin, J. Qin, J. Xu, W. Li, J. Xiong, J. Liu, Z. Xiao, K. Sun, *et al.*, 18% efficiency organic solar cells, *Sci. Bull.*, 2020, **65**, 272.

37 J. Yuan, Y. Zhang, L. Zhou, G. Zhang, H.-L. Yip, T.-K. Lau, X. Lu, C. Zhu, H. Peng, P. A. Johnson, *et al.*, Single-junction organic solar cell with over 15% efficiency using fused-ring acceptor with electron-deficient core, *Joule*, 2019, **3**, 1140.

38 J. Faisst, E. Jiang, S. Bogati, L. Pap, B. Zimmermann, T. Kroyer, U. Würfel and M. List, Organic solar cell with an active area> 1 cm2 achieving 15.8% certified efficiency using optimized vis-nir antireflection coating, *Sol. RRL*, 2023, **7**, 2300663.

39 M. Zhang, X. Guo, W. Ma, H. Ade and J. Hou, A large-bandgap conjugated polymer for versatile photovoltaic applications with high performance, *Adv. Mater.*, 2015, **27**, 4655.

40 Q. Fan, W. Su, Y. Wang, B. Guo, Y. Jiang, X. Guo, F. Liu, T. P. Russell, M. Zhang and Y. Li, Synergistic effect of fluorination on both donor and acceptor materials for high performance non-fullerene polymer solar cells with 13.5% efficiency, *Sci. China:Chem.*, 2018, **61**, 531.

41 S. Dong, T. Jia, K. Zhang, J. Jing and F. Huang, Single-component non-halogen solvent-processed high-

performance organic solar cell module with efficiency over 14%, *Joule*, 2020, **4**, 2004.

42 L. Perdigón-Toro, L. Q. Phuong, S. Zeiske, K. Vandewal, A. Armin, S. Shoaee and D. Neher, Excitons dominate the emission from pm6: Y6 solar cells, but this does not help the open-circuit voltage of the device, *ACS Energy Lett.*, 2021, **6**, 557.

43 J. Faisst, M. List, F. Heinz and U. Würfel, Direct determination of the steady state and time-resolved quasi-fermi level separation in organic solar cells from electroluminescence measurements, *Adv. Opt. Mater.*, 2022, **10**, 2200909.

44 F. D. Eisner, M. Azzouzi, Z. Fei, X. Hou, T. D. Anthopoulos, T. J. S. Dennis, M. Heeney and J. Nelson, Hybridization of local exciton and charge-transfer states reduces nonradiative voltage losses in organic solar cells, *J. Am. Chem. Soc.*, 2019, **141**, 6362.

45 M. List, J. Faisst, F. Heinz and U. Würfel, Determination of free charge carrier luminescence and quasi-fermi level separation in organic solar cells via transient photoluminescence measurements, *Adv. Opt. Mater.*, 2023, **11**, 2300895.

46 J. Faisst, M. List, C. Baretzky, A. W. Bett and U. Würfel, Implied voltage and current characterization in organic solar cells using transient photoluminescence, *Adv. Energy Mater.*, 2025, **15**, 2501348.

47 B. Sun, N. Tokmoldin, O. Alqahtani, A. Patterson, C. S. De Castro, D. B. Riley, M. Pranav, A. Armin, F. Laquai, B. A. Collins, *et al.*, Toward more efficient organic solar cells: a detailed study of loss pathway and its impact on overall device performance in low-offset organic solar cells, *Adv. Energy Mater.*, 2023, **13**, 2300980.

48 M. Pranav, A. Shukla, D. Moser, J. Rumeney, W. Liu, R. Wang, B. Sun, S. Smeets, N. Tokmoldin and F. Jaiser, *et al.*, On the Critical Competition between Singlet Exciton Decay and Free Charge Generation in Non-fullerene-based Organic Solar Cells with Low Energetic Offsets, *arXiv*, 2024, preprint arXiv:2404.03960, DOI: 10.48550/arXiv.2404.03960.

49 X. Zou, C. Ma, C. C. Chan, J. Zhang, Y. Li, A. Shang, Z. Wang, L. Arunagiri, Z. Qi, H. Ade, *et al.*, Optically probing field-dependent charge dynamics in non-fullerene organic photovoltaics with small interfacial energy offsets, *J. Phys. Chem. C*, 2021, **125**, 1714.

50 A. Petersen, A. Ojala, T. Kirchartz, T. A. Wagner, F. Würthner and U. Rau, Field-dependent exciton dissociation in organic heterojunction solar cells, *Phys. Rev. B Condens. Matter*, 2012, **85**, 245208.

51 Y. Liu, J. Zhang, G. Zhou, F. Liu, X. Zhu and F. Zhang, Electric field facilitating hole transfer in non-fullerene organic solar cells with a negative homo offset, *J. Phys. Chem. C*, 2020, **124**, 15132.

52 M. Más-Montoya and R. A. Janssen, The effect of h-and j-aggregation on the photophysical and photovoltaic properties of small thiophene–pyridine–dpp molecules for bulk-heterojunction solar cells, *Adv. Funct. Mater.*, 2017, **27**, 1605779.

53 J. Fang, Z. Wang, Y. Chen, Q. Zhang, J. Zhang, L. Zhu, M. Zhang, Z. Cui, Z. Wei, H. Ade, *et al.*, Revealing aggregation of non-fullerene acceptors in intermixed phase by ultraviolet-visible absorption spectroscopy, *Cell Rep. Phys. Sci.*, 2022, **3**, 100983.

54 S. Ge, L. Yang, Z. Wang, T. Du, Q. Guo, M. Liu, M. Du and E. Zhou, Tailoring aggregation behavior of shamrock-shaped non-fullerene acceptors via an isomerisation strategy enables high-performance organic solar cells, *J. Mater. Chem. A*, 2025, **13**, 27107.

55 M. List, T. Sarkar, P. Perkhun, J. Ackermann, C. Luo and U. Würfel, Correct determination of charge transfer state energy from luminescence spectra in organic solar cells, *Nat. Commun.*, 2018, **9**, 3631.

56 M. Azzouzi, N. P. Gallop, F. Eisner, J. Yan, X. Zheng, H. Cha, Q. He, Z. Fei, M. Heeney, A. A. Bakulin, *et al.*, Reconciling models of interfacial state kinetics and device performance in organic solar cells: impact of the energy offsets on the power conversion efficiency, *Energy Environ. Sci.*, 2022, **15**, 1256.

57 J. S. Müller, M. Comí, F. Eisner, M. Azzouzi, D. Herrera Ruiz, J. Yan, S. S. Attar, M. Al-Hashimi and J. Nelson, Charge-transfer state dissociation efficiency can limit free charge generation in low-offset organic solar cells, *ACS Energy Lett.*, 2023, **8**, 3387.